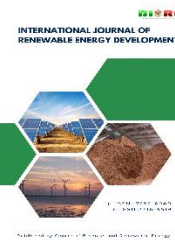




Contents list available at CBIORE journal website







**International Journal of Renewable Energy Development**

Journal homepage: <https://ijred.cbiorc.id>



Research Article

# Energy and exergy performance of a solar-driven $\text{NH}_3$ -NaSCN absorption refrigeration cycle: Case study in the Colombian Caribbean

Vanessa Carval-García<sup>a</sup> , Daniela Sabalza-Pérez<sup>a</sup> , Jean Caratt-Ortiz<sup>a\*</sup> , Nelly De Armas-Calderón<sup>a</sup> , Andrés Rodríguez-Toscano<sup>a</sup> , Howen Anguiano-González<sup>b</sup> 

<sup>a</sup>Energy Department, Faculty of Engineering, Universidad de la Costa, Barranquilla, 08002, Colombia

<sup>b</sup>Department of Mechanical Engineering, Faculty of Engineering, Instituto Tecnológico Superior de Puruándiro, Puruándiro, 58532, México

**Abstract.** Absorption refrigeration systems are increasingly recognized as sustainable alternatives for cooling applications, particularly when integrated with renewable energy sources such as solar thermal systems. Among the available working pairs, the  $\text{NH}_3$ -NaSCN solution offers favorable thermodynamic properties and low environmental impact; however, its performance under tropical climatic conditions with solar integration remains insufficiently explored. This study evaluates the thermodynamic and exergetic performance of a single-effect  $\text{NH}_3$ -NaSCN absorption refrigeration cycle integrated with a flat-plate solar collector, considering the climatic conditions of five cities of the Colombian Caribbean Region. A validated thermodynamic model was applied to assess the influence of generator, condenser, absorber, and evaporator temperatures on the coefficient of performance (COP) and exergetic efficiency. Results show that increasing generator temperature from 75 °C to 120 °C enhances COP by up to 46.15 %, while raising the evaporator temperature from -8 °C to 4 °C improves COP by 16 %. Conversely, increasing condenser and absorber temperatures reduce COP by 20.54 % and 16 %, respectively. Exergy destruction analysis indicates that the generator and absorber account for 55 % and 34 % of total irreversibilities, highlighting them as priority targets for optimization. Analysis of variance identified generator temperature as the most influential parameter on COP (39.37 %), followed by condenser (31.22 %) and evaporator temperatures (15.18 %). Solar integration enabled stable operation with an average COP decrease of only 3 % across the five cities; however, the use of water in the solar collector restricted operation below the optimal efficiency range (95–120 °C). The combined performance index integrating COP and exergetic efficiency showed that the operating range characterized by elevated generator temperature and reduced condenser temperature delivers the best energy–exergy trade-off, providing design guidelines for high-irradiance regions and supporting the adoption of  $\text{NH}_3$ -NaSCN as a cost-effective, renewable refrigeration solution.

**Keywords:** Absorption refrigeration system,  $\text{NH}_3$ -NaSCN, exergy analysis, solar thermal integration, energy–exergy optimization, Ammonia–sodium thiocyanate



© The author(s). Published by CBIORE. This is an open access article under the CC BY-SA license (<https://creativecommons.org/licenses/by-sa/4.0/>).

Received: 13<sup>th</sup> August 2025; Revised: 17<sup>th</sup> Dec 2025; Accepted: 20<sup>th</sup> January 2026; Available online: 5<sup>th</sup> February 2026

## 1. Introduction

In recent years, energy efficiency has gained significant importance across industrial sectors as a means to optimize operational models, enhance competitiveness and operational performance, and reduce costs. This is achieved through the implementation of technological innovations and best practices aimed at minimizing energy consumption, thereby contributing to environmental sustainability and compliance with regulatory standards (Ali & Evans, 2025).

In this context, the growing demand for energy-efficient and sustainable solutions has led to increasing interest in refrigeration technologies, particularly absorption refrigeration systems. One of the most distinctive features of these systems is their ability to operate using thermal energy rather than electrical power (Velázquez Martí, 2017), (Soto Robles, 2018), (Ramírez Álvarez *et al.*, 2015), positioning them as a promising alternative to conventional vapor-compression refrigeration technologies. However, the efficiency of absorption cycles remains a critical aspect, as these systems must maximize the

utilization of available thermal energy in order to be competitive with conventional compression-based technologies. The improvement of both energy and exergy efficiency in these systems can be achieved through the optimization of the thermodynamic properties of the working mixtures, the integration of heat exchangers, and the adjustment of the refrigerant concentration ratio (Takalkar & Sleiti, 2022).

Single-effect absorption refrigeration systems operate with two types of substances: a refrigerant, which evaporates and absorbs heat from the surroundings to produce the cooling effect, and an absorbent, which is responsible for absorbing the refrigerant in its vapor phase (Cabrera César *et al.*, 2021). The most commonly used binary working mixtures for these systems in both industrial and residential applications include  $\text{NH}_3$ -LiNO<sub>3</sub>,  $\text{NH}_3$ -H<sub>2</sub>O, LiBr-H<sub>2</sub>O,  $\text{NH}_3$ -NaSCN (Velázquez Martí, 2017), (Soto Robles, 2018), (Cabrera César *et al.*, 2021), (Ngock *et al.*, 2020).

The increasing demand for low-carbon-footprint systems, driven by growing environmental concerns, has intensified interest in alternative working pairs such as  $\text{NH}_3$ -NaSCN. In this

\* Corresponding author  
Email: [jcaratt@cuc.edu.co](mailto:jcaratt@cuc.edu.co) (J. Carrat-Ortiz)

context, Velázquez Martí (2017) and his team conducted a comprehensive study on single-effect absorption refrigeration systems employing  $\text{NH}_3\text{-NaSCN}$  as the working fluid pair, with a particular focus on evaluating their thermodynamic performance and overall efficiency. Using mathematical models and numerical simulations, they analyzed both the energy performance and the exergy losses in key system components, including the generator, absorber, condenser, and evaporator. Their findings highlighted the optimization of the refrigerant concentration ratio and the integration of heat exchangers as critical strategies for enhancing the overall efficiency of the system.

The  $\text{NH}_3\text{-NaSCN}$  working pair has demonstrated the potential to achieve higher coefficients of performance (COP) under similar operating conditions compared to traditional  $\text{NH}_3\text{-H}_2\text{O}$  (Shankar *et al.*, 2017) and  $\text{LiBr-H}_2\text{O}$  systems (Waghare & Sathyabhama, 2022). In addition to its superior thermodynamic performance, this mixture offers relevant economic and operational advantages, as it is approximately eight times less expensive than  $\text{NH}_3\text{-LiNO}_3$  and exhibits better energy efficiency than the  $\text{NH}_3\text{-H}_2\text{O}$  mixture at an evaporator temperature of 7 °C. Owing to its lower viscosity, two to three times lower than that of  $\text{NH}_3\text{-LiNO}_3$ , the use of  $\text{NH}_3\text{-NaSCN}$  may allow for reduced heat exchange surface requirements and smaller solar collector areas without significantly affecting the COP (Ramírez Álvarez *et al.*, 2015), (Ngock *et al.*, 2020). Moreover, systems employing  $\text{NH}_3\text{-NaSCN}$  can operate at lower generator and evaporator temperatures, which enhances their suitability for low-grade heat sources such as solar energy or industrial waste heat (Ngock *et al.*, 2020), (Rabiei *et al.*, 2024). From a system design perspective,  $\text{NH}_3\text{-NaSCN}$  also presents an important structural advantage: unlike  $\text{NH}_3\text{-H}_2\text{O}$  systems, which require a rectifier to remove water vapor from the refrigerant before it enters the condenser, absorption refrigeration systems using  $\text{NH}_3\text{-NaSCN}$  do not require this component, as the salt-based absorbent does not evaporate with the refrigerant. This characteristic simplifies the system configuration and reduces both complexity and equipment cost (Rabiei *et al.*, 2024), (Zhu & Gu, 2010). The advantages of the  $\text{NH}_3\text{-NaSCN}$  mixture, including its lower cost and superior energy efficiency, translate into practical applications with enhanced system reliability and economic feasibility. For instance, in remote regions where electricity is scarce or expensive, absorption refrigeration systems powered by solar energy or industrial waste heat can offer an effective cooling solution for homes, clinics and food storage facilities (Niño Villamizar *et al.*, 2023).

Despite the favorable thermodynamic, economic, and operational characteristics of the  $\text{NH}_3\text{-NaSCN}$  working pair, most existing studies have focused on theoretical analyses or idealized operating conditions, with limited attention to its performance under realistic, location-specific climatic scenarios. In particular, the application of  $\text{NH}_3\text{-NaSCN}$  absorption refrigeration systems driven by solar energy remains scarcely explored when compared to conventional working pairs such as  $\text{LiBr-H}_2\text{O}$  and  $\text{NH}_3\text{-H}_2\text{O}$ . This lack of studies under real local conditions restricts the assessment of the practical feasibility and performance limits of  $\text{NH}_3\text{-NaSCN}$ -based systems, especially in regions with high solar potential and limited access to conventional electricity.

The main objective of this study is to conduct an energy and exergy analysis of a single-effect absorption refrigeration cycle using  $\text{NH}_3\text{-NaSCN}$  as the working fluid pair, with a particular focus on evaluating the system's performance under realistic local operating conditions. Although  $\text{NH}_3\text{-NaSCN}$  has been identified as a promising alternative working pair, its

application in absorption refrigeration systems has not yet been widely assessed under realistic operating conditions.

To address this gap, the present study integrates a solar collector into the absorption refrigeration system and evaluates its behavior using average solar irradiance vectors corresponding to five Caribbean cities in Colombia. The collected solar energy is employed to heat a thermal fluid stored in a tank, which subsequently supplies the generator to drive the ammonia evaporation process. While this methodological framework has been widely applied to  $\text{LiBr-H}_2\text{O}$  systems under local climatic conditions (Toscano, Ortiz, & Calderón, 2024), (Toscano, Ortiz, Armas Calderón, *et al.*, 2024), (Camara & Sulin, 2024), (Alshammari, 2025), (Bouzyan *et al.*, 2023), (Bastos & Almeida, 2024), only a single study has reported its application to  $\text{NH}_3\text{-NaSCN}$  systems, and this was conducted under local conditions in India (Modi, Pandya, Kumar, *et al.*, 2020). To the authors' knowledge, no previous studies have evaluated a solar-driven  $\text{NH}_3\text{-NaSCN}$  absorption refrigeration system under the specific climatic conditions of the Colombian Caribbean region.

By combining energy and exergy analyses with location-specific solar data, this work provides new insights into the performance and applicability of  $\text{NH}_3\text{-NaSCN}$  absorption systems in tropical coastal environments. The results contribute to reducing the existing knowledge gap regarding this working pair and support its potential implementation in regions with high solar availability and limited access to conventional electricity.

The remainder of this paper presents the methodological framework adopted for the analysis of a solar-assisted absorption refrigeration system, including the system configuration, thermodynamic modeling, and the formulation of the energy and exergy analyses. The model validation and a detailed discussion of the results are then provided, addressing the coefficient of performance, exergy behavior, solar-assisted operation, and optimization using the Response Surface Method. The main conclusions of the study are finally summarized.

## 2. Methodology.

### 2.1. Description of the System

Absorption refrigeration systems operate based on a thermodynamic cycle that exploits the ability of certain working fluids to absorb and release a refrigerant. Unlike mechanical compression systems, absorption systems use a heat source to separate the refrigerant from the absorbent, eliminating the need for a mechanical compressor. As shown in Figure 1, the absorption refrigeration cycle begins in the generator, where thermal energy is supplied to the refrigerant-absorbent solution. In the present investigation,  $\text{NH}_3\text{-NaSCN}$  pair is employed as the working fluid of the system. The heat input causes the refrigerant (ammonia) to separate from the absorbent (sodium thiocyanate) in vapor form (Isaza-Roldan & Cardona-Gil, 2014).

Following its separation in the generator, the refrigerant vapor enters the condenser, where it releases latent heat to the surroundings and condenses into a liquid phase. The high-pressure liquid then passes through an expansion valve, where a significant drop in pressure and temperature occurs. This low-pressure refrigerant subsequently enters the evaporator, where it undergoes phase change by absorbing heat from the surroundings, thereby producing a cooling effect. The resulting refrigerant vapor is then absorbed by a liquid solution in the absorber, forming a mixture enriched in refrigerant. This solution is directed to the generator, where it is heated by an

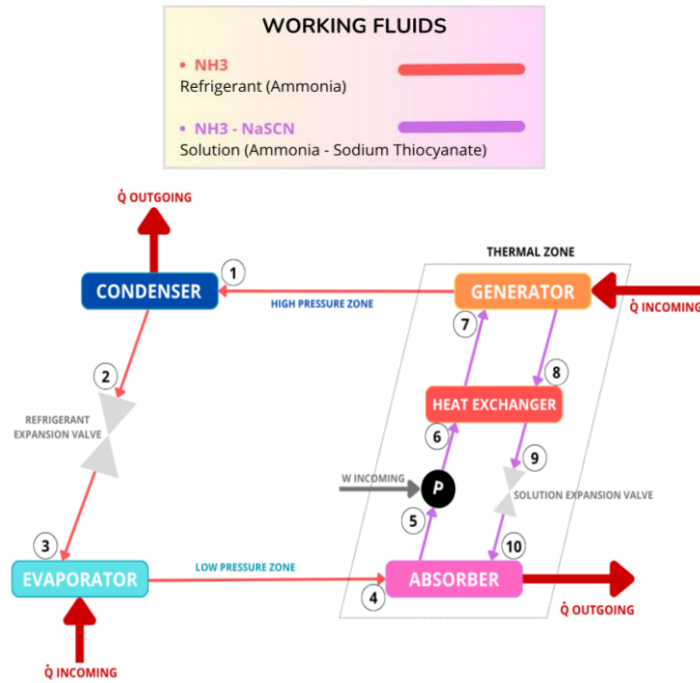


Fig. 1 NH<sub>3</sub>-NaSCN absorption refrigeration system.

external thermal source, triggering the desorption of the refrigerant in vapor form and completing the cycle.

In absorption refrigeration systems using NH<sub>3</sub>-H<sub>2</sub>O, a rectifier is required to remove water vapor from the ammonia before it enters the condenser. However, in systems employing NH<sub>3</sub>-NaSCN, a rectifier is not necessary, as the salt-based absorbent does not evaporate with the refrigerant, thereby simplifying the system design and reducing both complexity and equipment cost (Rabiei *et al.*, 2024), (Zhu & Gu, 2010). This system demonstrates high efficiency when driven by waste heat or renewable energy sources, enabling its application in industrial processes and air-conditioning systems without the need for complex mechanical components (Mardones Barrientos, 2016).

The absorption system employing the NH<sub>3</sub>-NaSCN working pair operates within a generator temperature range of 87 °C to 115 °C, which enables improved thermal efficiency compared to other refrigerant-absorbent combinations (Modi, Pandya, & Patel, 2020). The operating pressure ranges between 0.2 and 0.5 MPa, depending on the system configuration and operating conditions (Siddiqui, 1993). These characteristics make the mixture suitable for industrial and commercial applications where efficient cooling is required using medium-temperature heat sources.

The NH<sub>3</sub>-NaSCN mixture exhibits high ammonia solubility in the absorbent, which enhances the absorption capacity and minimizes the need for rectification stages within the system. Additionally, its coefficient of performance (COP) is higher than that of the NH<sub>3</sub>-H<sub>2</sub>O pair, reaching values close to 0.7 under optimal operating conditions (Sun, 1998). The chemical stability of the mixture, along with its low tendency to crystallize, enables more reliable and extended system operation, mitigating common issues encountered in other absorption refrigeration cycles.

### 2.2. Thermodynamic properties

The thermodynamic properties of ammonia were obtained through MATLAB using the CoolProp library, an open-access tool that offers a comprehensive set of correlations and

equations of state for numerous pure and pseudo-pure substances (Bell *et al.*, 2014). Although CoolProp provides reliable data for pure ammonia, it does not include the specific NH<sub>3</sub>-NaSCN mixture. Consequently, the thermophysical properties of the NH<sub>3</sub>-NaSCN solution were coded manually, following the correlations and tabulated values found in the relevant scientific literature.

The thermodynamic properties of ammonia were determined using an equation of state expressed explicitly in terms of the Helmholtz free energy, formulated as a function of temperature and density (Gao *et al.*, 2023). This formulation enables the consistent calculation of all thermodynamic properties through analytical derivatives of the Helmholtz energy and is especially well-suited for describing fluids with complex behaviors such as molecular association.

The total molar Helmholtz energy  $a(T, \rho)$  is separated into two contributions:

$$a(T, \rho) = a^o(T, \rho) + a^r(T, \rho) \tag{1}$$

Where  $a^o$  is the ideal-gas molar Helmholtz energy and  $a^r$  is the residual molar Helmholtz energy, corresponding to real-fluid contribution.

The ideal-gas component of the Helmholtz energy was derived by integrating thermodynamic relations using the temperature-dependent ideal gas heat capacity  $c_p^o(T_o)$ . The molar enthalpy  $h^o$  and entropy  $s^o$  were evaluated with respect to a reference state  $(T_o, p_o)$  using the following expressions:

$$h^o(T) = h^o(T_o) + \int_{T_o}^T C_p^o(T_o) dT \tag{2}$$

$$s^o(T, \rho) = s_o^o(T_o, p_o) + \int_{T_o}^T \frac{C_p^o(T_o) - R}{T} dT - R \cdot \ln\left(\frac{\rho}{\rho_o}\right) \tag{3}$$

These results were then combined to obtain the ideal-gas Helmholtz energy:

$$a^o(T, \rho) = h^o(T) - RT - Ts^o(T, \rho) \tag{4}$$

The ideal-gas density is defined at the same state, where  $\rho_0^o = \frac{p_0}{R \cdot T_0}$ . For consistency and reproducibility, the reference conditions were chosen as  $T_0 = 300\text{ K}$  y  $p_0 = 1.0\text{ kPa}$ .

The residual Helmholtz energy  $a^r(T, \rho)$  accounts for real-fluid behavior and was constructed from a summation of terms including polynomial, exponential, and Gaussian bell-shaped functions. This structure enables high flexibility for representing the complex behavior of ammonia, particularly near the critical point and in regions affected by molecular association.

The general form used is:

$$\alpha^r(\tau, \delta) = \alpha_{Pol}^r + \alpha_{Exp}^r + \alpha_{GBS}^r \tag{5}$$

$$\alpha^r(\tau, \delta) = \sum_{i=1}^{I_{Pol}} n_i \delta^{d_i} \tau^{t_i} + \sum_{i=I_{Pol}+1}^{I_{Pol}+I_{Exp}} n_i \delta^{d_i} \tau^{t_i} \exp(-r_i \delta^{l_i}) + \sum_{i=I_{Pol}+I_{Exp}+I_{GBS}}^{I_{Pol}+I_{Exp}+I_{GBS}} n_i \delta^{d_i} \tau^{t_i} \exp[-\eta_i(\delta - \varepsilon_i)^2 - \beta_i(\tau - \gamma_i)^2] \tag{6}$$

where  $I_{Pol}$ ,  $I_{Exp}$ , and  $I_{GBS}$  are the number of polynomial-like terms, exponential terms, and Gaussian bell-shaped terms, respectively.  $\delta = \frac{\rho}{\rho_c}$  and  $\tau = \frac{T_c}{T}$  are the reduced density and inverse reduced temperature, respectively, and the coefficients  $n_i, d_i, t_i, l_i$  were fitted to experimental data. All thermodynamic properties can be calculated as derivatives of the Helmholtz energy from Eqs. (4) and (6) as explained by Lemmon et al. (2009).

These relations were applied throughout the temperature range from the triple point (195.49 K) up to 725 K and at pressures up to 1000 MPa, ensuring consistency and physical accuracy across all relevant thermodynamic states. The thermophysical properties of the ammonia–sodium thiocyanate ( $\text{NH}_3\text{-NaSCN}$ ) solution were originally investigated by Infante Ferreira (1984), whose equations were subsequently presented in a more explicit and usable form by Zhu & Gu (2010).

The relation among saturation equilibrium pressure, concentration and temperature is given as:

$$\ln P = A + \frac{B}{T} \tag{7}$$

Where,

$$A = 15.7266 - 0.298628X \tag{8}$$

$$B = -2548.65 - 2621.92(1 - X)^3 \tag{9}$$

The relation among temperature, concentration and enthalpy is as follows:

$$h = A + B(T - 273.15) + C(T - 273.15)^2 + D(T - 273.15)^3 \tag{10}$$

Where,

$$A = 79.72 - 1072X + 1287.9X^2 - 295.67X^3 \tag{11}$$

$$B = 2.4081 - 2.2814X + 7.9291X^2 - 3.5137X^3 \tag{12}$$

$$C = 10^{-2}(1.255X - 4X^2 + 3.06X^3) \tag{13}$$

$$D = 10^{-5}(-3.33X + 10X^2 - 3.33X^3) \tag{14}$$

For the specific entropy of Ammonia/NaSCN solution, the present work have calculated the values using the corrected correlated equation proposed by Farshi et al. (2014) as follows:

**Table 1**

Constant values for calculating specific entropy

Constant Symbol	Constant Values
a	$-1.88297 \cdot 10^{-1}$
b	1.04668
c	$3.73268 \cdot 10^{-3}$
d	$-4.47284 \cdot 10^{-5}$
e	$1.98330 \cdot 10^{-7}$
f	$-1.32557 \cdot 10^{-1}$
g	$-8.99647 \cdot 10^{-3}$
h	$5.16364 \cdot 10^{-5}$
i	$-1.16584 \cdot 10^{-7}$

$$s = (a + b \cdot X + c \cdot T + d \cdot T^2 + e \cdot T^3) / (1 + f \cdot X + g \cdot T + h \cdot T^2 + i \cdot T^3) \tag{15}$$

The constant values for Eq. (15) are shown in Table 1.

### 2.3. Thermodynamic analysis

Based on the mass conservation principle and assuming steady-state conditions for all components of the VAR system, the conservation laws of mass (Equation 16), species (Equation 17), and energy (Equation 18) were applied.

$$\sum \dot{m}_{in} - \sum \dot{m}_{out} = 0 \tag{16}$$

$$\sum \dot{m}_{in} \cdot X_{in} - \sum \dot{m}_{out} \cdot X_{out} = 0 \tag{17}$$

$$\sum \dot{m}_{in} \cdot h_{in} - \sum \dot{m}_{out} \cdot h_{out} - \sum \dot{Q} + \sum \dot{W} = 0 \tag{18}$$

It is widely accepted in the analysis of this cycle that the refrigerant leaving the generator and entering the condenser is free of sodium thiocyanate (Ngock *et al.*, 2022). Accordingly, the refrigerant at this point is considered a pure stream of ammonia, leading to:

$$X_1 = 1 \tag{19}$$

which means that for a concentration  $X = 1$ , there is pure ammonia, while a concentration  $X$  below 1 means that there is an amount  $1 - X$  of sodium thiocyanate in the mixture.

The outlet streams from the generator, absorber, condenser, and evaporator are assumed to be in saturated conditions. Specifically, the solution exiting the generator toward the heat exchanger, as well as the stream from the absorber to the pump, are both considered saturated liquid solutions. In the case of the condenser, the refrigerant (ammonia) is assumed to exit as saturated liquid. Meanwhile, the stream leaving the evaporator is considered saturated vapor, corresponding to pure ammonia. The input data defined for the simulation represent typical operating conditions of a single-effect absorption refrigeration system employing an ammonia–sodium thiocyanate ( $\text{NH}_3\text{-NaSCN}$ ) working pair. The temperatures of the generator, condenser, evaporator, and absorber are specified and varied within defined intervals, and expressed in Kelvin to ensure consistency in thermodynamic computations. The selected temperature ranges for each component were established based on the operating conditions reported in previous studies by Rabiei *et al.*, (2024), Zhu & Gu (2010) and Pandya *et al.* (2019). For validation purposes, the mass flow rates of ammonia and sodium thiocyanate are set to 0.0038 kg/s and 0.0262 kg/s, respectively, resulting in a total solution flow rate of 0.03 kg/s. The effectiveness of the internal heat exchangers is assumed to be 0.8, and the specific volume of the solution is approximated as 0.0006 m<sup>3</sup>/kg.

The total flow exergy  $\psi$  of a state, considering that potential and kinetic components are negligible, is calculated taken into account only the physical exergy of a flow  $\psi_{ph}$  which represents the maximum useful work obtainable as the system transitions from an initial state defined by temperature and pressure ( $T, p$ ) to a reference state ( $T_0, p_0$ ) through a reversible process that interacts solely with the environment at reference conditions. This quantity is determined by the following expression:

$$\psi_{ph} = (h - h_0) - T_0(s - s_0) \tag{20}$$

where  $h$  and  $s$  denote the specific enthalpy and entropy, respectively, with the subscript zero indicating evaluation at the dead state under reference temperature ( $T_0$ ). For pure ammonia, this expression is governed by temperature and pressure, while in the  $\text{NH}_3\text{-NaSCN}$  solution, it also depends on the mixture concentration. Given the absence of a standardized chemical exergy value for NaSCN and the fact that no chemical reactions occur within the ammonia/salt absorption refrigeration system, the chemical exergy of the ammonia-sodium thiocyanate solution was not considered in this analysis (Rabiei *et al.*, 2024), (Cai *et al.*, 2014). After the determination of the total flow exergy  $\psi$ , the total exergy expressed in terms of rate, is obtained by multiplying the total flow exergy with the flow rate of that state:

$$\dot{E} = \dot{m} \cdot \psi \tag{21}$$

The exergetic efficiency of the system refers to the proportion of the desired output exergy to the overall exergy input of the system.

#### 2.4. Solar Collector

The modeling of the flat plate solar collector is based on the equations presented by Duffie & Beckman (2013) and Kerme *et al.* (2017). The rate of useful energy transferred by the collector is defined as:

$$\dot{Q}_u = A_c I_T \eta_c \tag{22}$$

where  $\dot{Q}_u$  is the useful energy collected by the solar system,  $A_c$  is the collector area,  $I_t$  is the total solar radiation incident on the collector and  $\eta_c$  is the instantaneous efficiency of the collector, which is defined as the ratio of useful heat gain over a given time period to the incident solar irradiation energy over the same period. The instantaneous efficiency of the collector is defined as:

$$\eta_c = F_R(\tau\alpha) - F_R U_L \frac{(T_{f,in} - T_a)}{I_T} \tag{23}$$

Where  $F_R U_L$  is the collector heat removal factor, which is calculated as the ratio between the actual rate of heat transfer to the working fluid and the rate of heat transfer that would occur if the entire absorber were at the minimum temperature difference between the collector absorber surface and the ambient air. Meanwhile,  $\tau\alpha$  is the transmittance-absorptance product, or optical efficiency, where the transmittance  $\tau$  is the fraction of incident solar radiation transmitted through the collector cover and the absorptance  $\alpha$  is the fraction of incident solar radiation absorbed by the collector absorber surface.  $U_L$  is the overall heat loss coefficient,  $T_{f,in}$  is the inlet temperature of the fluid entering the collector and  $T_a$  is the ambient temperature. Typically, the products  $F_R(\tau\alpha)$  y  $F_R U_L$  are characteristic parameters for a given solar collector and govern its thermal performance. These values are tabulated and obtained from experimental data using a graphical representation of the collector efficiency  $\eta_c$  versus  $\frac{(T_{f,in} - T_a)}{I_T}$  where  $F_R(\tau\alpha)$  is the y-intercept and  $F_R U_L$  is the slope (Duffie & Beckman, 2013).

Concerning solar irradiation, data were collected for five cities in the Colombian Caribbean region: Barranquilla, Santa Marta, Cartagena, Riohacha, and Valledupar; using the PV\*SOL application. PV\*SOL is a specialized software for the simulation and sizing of photovoltaic systems, widely used in academic research and solar energy projects due to its accuracy in modeling real-world radiation and performance conditions (Raugei & Frankl, 2009). This tool enables the estimation of available solar energy by accounting for specific climatological and geographical variables, which is essential for assessing the photovoltaic generation potential in different areas (Kabir *et al.*, 2018). The data used in the present study is presented in Table 2.

#### 2.5. Storage tank modelling

The storage tank is integrated into the solar collection system with the purpose of retaining the captured thermal energy and ensuring a continuous heat supply during periods of insufficient solar irradiance. For modeling purposes, it is assumed that the water within the insulated tank is perfectly mixed with the return streams from both the collector and the generator. Assuming complete mixing and thermal homogeneity within the tank, the resulting energy balance is expressed as follows (Duffie & Beckman, 2013):

**Table 2**  
Incident radiation vector – irradiance ( $W/m^2$ )

TIME	CITY				
	Barranquilla	Santa Marta	Cartagena	Valledupar	Riohacha
6:00	90.23	91.45	91.73	89.97	94.36
7:00	136.19	137.18	137.59	134.96	141.53
8:00	226.99	228.63	229.32	224.93	235.89
9:00	363.18	365.81	366.90	359.89	377.42
10:00	453.97	457.26	458.63	449.86	471.78
11:00	544.77	548.71	550.36	539.84	566.14
12:00	544.77	548.71	550.36	539.84	566.14
13:00	544.77	548.71	550.36	539.84	566.14
14:00	453.97	457.26	458.63	449.86	471.78
15:00	363.18	365.81	366.99	359.89	377.42
16:00	226.99	228.63	229.32	224.93	235.89
17:00	136.19	137.18	137.59	134.96	141.53
18:00	90.79	91.45	91.73	89.97	94.36

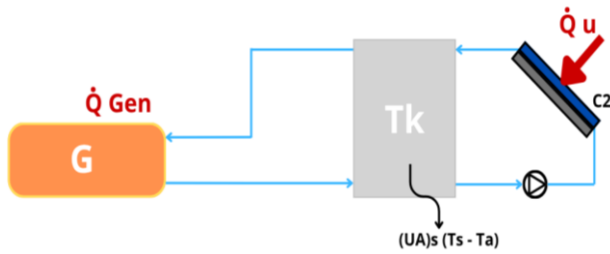


**Fig. 2** Solar collector and storage tank coupled to the generator.

$$\left[ (mC_p)_s \right] \frac{dT_s}{dt} = \dot{Q}_u - Q_{load} - (UA)_s(T_s - T_a) \quad (24)$$

Where  $m$  is the mass of water in the storage tank,  $C_p$  is the specific heat capacity of water and  $T_a$  is the ambient temperature surrounding the tank. In this model  $\dot{Q}_u$  and  $Q_{load}$  represent the useful thermal energy extracted from the solar collector and the energy required by the absorption refrigeration system (i.e., the thermal load demanded by the generator), respectively. Additionally,  $(UA)_s$  represents the overall heat loss coefficient of the storage tank, which quantifies heat losses per unit temperature difference and is taken as  $11.1 \frac{W}{C}$  (Kerme *et al.*, 2017). If  $\dot{Q}_u$ ,  $Q_{load}$  and the tank's heat losses over a time interval  $\Delta t$  are assumed to remain constant, Equation (25) can be rewritten for each interval as follows:

$$T_{s,new} = T_s + \frac{\Delta t}{mC_p} [\dot{Q}_u - Q_{load} - (UA)_s(T_s - T_a)] \quad (25)$$

Where  $T_{s,new}$  is the temperature of the storage tank at the end of the time Interval  $\Delta t$  and  $T_s$  is the tank temperature during the Interval  $\Delta t$ . At the end of each time step, the value of  $T_{s,new}$  is assigned as the new  $T_s$  for the subsequent interval, and this procedure is repeated iteratively over the entire simulation period. The solar collector and storage tank coupled to the system are shown in Figure 2.

## 2.6. Performance indicators

The coefficient of performance (COP) is the key indicator used to quantify the efficiency of single-effect absorption refrigeration systems powered by solar energy. It is defined as the ratio between the cooling effect produced in the evaporator and the total thermal energy supplied to the generator, which sometimes includes the energy consumed by the solution pump. In a solar-driven absorption cycle, a high COP reflects a more efficient conversion of thermal energy into useful cooling capacity, which is essential for assessing different configurations, operating conditions, and energy-saving potential. This parameter enables meaningful comparisons between systems and serves as a basis for optimizing both the design and integration of the solar collector.

$$COP = \frac{\dot{Q}_{eva}}{\dot{Q}_{gen} + \dot{W}_{pump}} \quad (26)$$

Exergy efficiency represents a more rigorous criterion than COP for evaluating absorption refrigeration systems, as it accounts for the system's ability to convert the supplied thermal energy into useful cooling while considering internal irreversibilities. Several studies have shown that there is an optimal generator temperature range at which exergy efficiency is maximized,

which is crucial for the efficient design and operation of these systems under varying conditions and thermal energy sources, such as solar power. Ngock *et al.* (2022) analyzed a single-effect absorption refrigeration system using  $NH_3$ - $NaSCN$  as the working pair and found that both COP and exergy efficiency reach their maximum values when the generator temperature is maintained between 92 °C and 100 °C. Other authors, such as Modi, Pandya, & Patel (2020), have identified a broader operating range, from 87 °C to 115 °C, which allows favorable system performance without compromising thermal stability or increasing the risk of crystallization. It is calculated as follows:

$$\eta = \frac{\dot{Q}_{eva} \left( \frac{T_0}{T_{eva}} - 1 \right)}{\dot{Q}_{gen} \left( 1 - \frac{T_0}{T_{gen}} \right) + \dot{W}_{pump}} \quad (27)$$

In addition to COP and exergy efficiency, the Solar Coefficient of Performance (SCOP) is increasingly used to evaluate the real-world performance of solar-driven cooling systems (Venegas *et al.*, 2020). SCOP represents the system's overall energy efficiency over a typical operating period (e.g., a day or season) by relating the total cooling output to the total solar energy incident on the collector surface during the same period. Its formulation is expressed as:

$$SCOP = \frac{\dot{Q}_{eva}}{\dot{Q}_{collector} + \dot{W}_{pump}} \quad (28)$$

## 2.7. Operational parameters

In this study, the effectiveness of the solution heat exchanger is assumed to be 0.80. Most of the analyses are conducted with condenser and evaporator temperatures of 25 °C. The refrigerant mass flow rate of ammonia is taken as  $\dot{m}_{NH_3} = 0.0038 \frac{kg}{s}$ , while that of sodium thiocyanate is  $\dot{m}_{NaSCN} = 0.0262 \frac{kg}{s}$  (Zhu & Gu, 2010). Regarding the solar sub-system, an array of collectors with a total area of  $A_C = 20 m^2$  is considered, with a collector heat removal factor of  $F_R U_L = 3.3 \frac{W}{m^2 \cdot C}$ , a storage tank volume of 5  $m^3$  and an emission-to-absorption factor  $F_R(\tau\alpha) = 0.70$  (Cabrera César *et al.*, 2021). The overall heat loss coefficient of the storage tank is  $(UA)_s = 11.1 \frac{W}{C}$  (Kerme *et al.*, 2017) and the average ambient temperature is assumed to be 25 C.

## 3. Validation

First, the enthalpy values obtained were validated against the work of Zhu & Gu (2010). The results shown in Figure 3 reveal noticeable discrepancies at states 1, 2, 3, and 4, where pure ammonia is present, with a maximum relative error of 46.63%. This deviation is attributed to the use of a conventional correlation in the reference study (Zhu & Gu, 2010), which may not fully capture the thermodynamic behavior of pure ammonia under the evaluated conditions. In contrast, the present investigation employs a more sophisticated approach, based on updated thermophysical property data and improved correlation techniques described by Gao *et al.* (2023), which significantly enhances the accuracy of the enthalpy predictions. For the states where the ammonia-salt solution is present, the agreement between the model and the reference data is nearly exact, demonstrating the robustness of the proposed methodology in capturing the mixture's thermodynamic behavior.

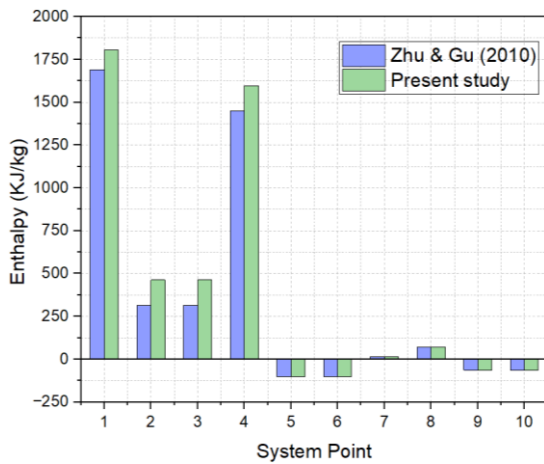


Fig. 3 Enthalpy validation.

The entropy values predicted by the present model, as shown in Figure 4, were validated against the reference data reported by Rabiei *et al.*, (2024), following the same comparative approach applied in the enthalpy assessment. The results reveal discrepancies at states 1, 2, 3, and 4, which correspond to the region where pure ammonia is present, with a maximum relative error of 30.87%. These deviations are consistent with those observed during the enthalpy validation and highlight the limitations of the conventional correlations employed in earlier studies. To address this issue, the present study adopts a more recent and experimentally supported correlation developed by Gao *et al.* (2023) to improve the representation of pure ammonia's thermodynamic behavior. For states 5 to 10, corresponding to the region where the ammonia-salt solution is present, the predicted entropy values exhibit near-perfect agreement with those reported by Rabiei *et al.*, (2024), reinforcing the consistency and robustness of the proposed methodology for modeling the working solution.

The statistical error analysis further supports the reliability of the proposed thermodynamic model. Based on the comparison with reference data, the Mean Absolute Error (MAE) (Eq. 29) and the Root Mean Square Error (RMSE) (Eq. 30) were evaluated for both enthalpy and entropy across all system states. The MAE represents the average magnitude of the absolute deviations between predicted and reference values, while the RMSE gives greater weight to larger discrepancies, providing a more conservative assessment of model accuracy. (Sharma & Maithani, 2026). The corresponding MAE and RMSE values are summarized in Table 3. For the

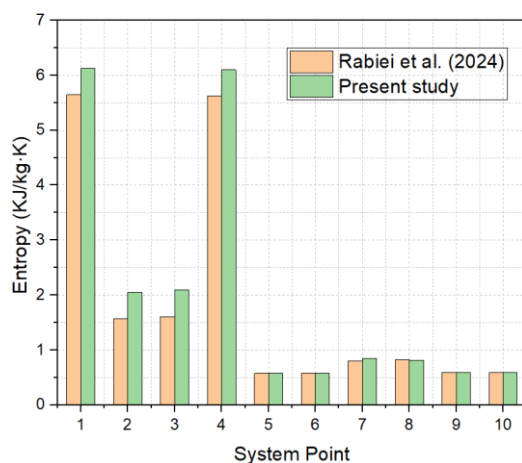


Fig. 4 Entropy validation.

Table 3

MAE and RMSE for enthalpy and entropy predictions.

Property	Region	MAE	RMSE	Units
Enthalpy	Pure NH <sub>3</sub> (States 1–4)	138.95	139.64	kJ kg <sup>-1</sup>
Enthalpy	NH <sub>3</sub> -NaSCN solution (States 5–10)	0.28	0.47	kJ kg <sup>-1</sup>
Enthalpy	All States	55.75	88.32	kJ kg <sup>-1</sup>
Entropy	Pure NH <sub>3</sub> (States 1–4)	0.48	0.48	kJ kg <sup>-1</sup>
Entropy	NH <sub>3</sub> -NaSCN solution (States 5–10)	0.01	0.02	kJ kg <sup>-1</sup>
Entropy	All States	0.20	0.31	kJ kg <sup>-1</sup>

NH<sub>3</sub>-NaSCN solution region (states 5–10), the errors are very low, with enthalpy MAE and RMSE of 0.28 and 0.47 kJ kg<sup>-1</sup> and entropy MAE and RMSE of 0.01 and 0.02 kJ kg<sup>-1</sup> K<sup>-1</sup>, confirming the near-perfect agreement observed in Figures 3 and 4. Higher error levels are observed for pure ammonia states (states 1–4), with enthalpy MAE and RMSE of 138.95 and 139.64 kJ kg<sup>-1</sup> and entropy MAE and RMSE of 0.48 kJ kg<sup>-1</sup> K<sup>-1</sup>, which is consistent with the limitations of conventional thermophysical property correlations for pure ammonia. When all system states are considered, the overall errors remain moderate for enthalpy (MAE = 55.75 kJ kg<sup>-1</sup> and RMSE = 88.32 kJ kg<sup>-1</sup>) and low for entropy (MAE = 0.20 kJ kg<sup>-1</sup> K<sup>-1</sup> and RMSE = 0.31 kJ kg<sup>-1</sup> K<sup>-1</sup>), and do not affect the predicted thermodynamic trends or the accuracy of system-level performance indicators such as COP and exergetic efficiency, confirming the robustness of the proposed model under the evaluated operating conditions.

$$MAE = \frac{1}{n} \sum_{i=1}^n |x_i^{model} - x_i^{reference}| \quad (29)$$

$$RMSE = \sqrt{\frac{1}{n} \sum_{i=1}^n (x_i^{model} - x_i^{reference})^2} \quad (30)$$

## 4. Results and discussion

### 4.1. Coefficient of Performance (COP)

Figure 5 shows the influence of generator temperature on the coefficient of performance (COP) of the system under investigation, considering different evaporator temperatures. As observed, the COP increases with generator temperature. This behavior can be explained by the thermodynamic effect of elevated generator temperatures, which supply more energy to drive the separation of the refrigerant (NH<sub>3</sub>) from the absorbent (NaSCN). This increases the concentration gradient between the strong and weak solutions, thereby enhancing the

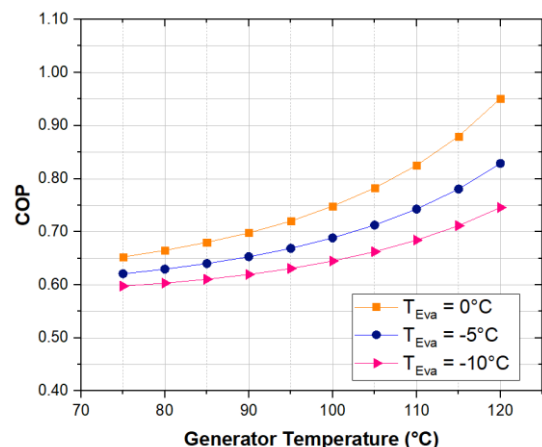


Fig. 5 COP vs Generator Temperature.

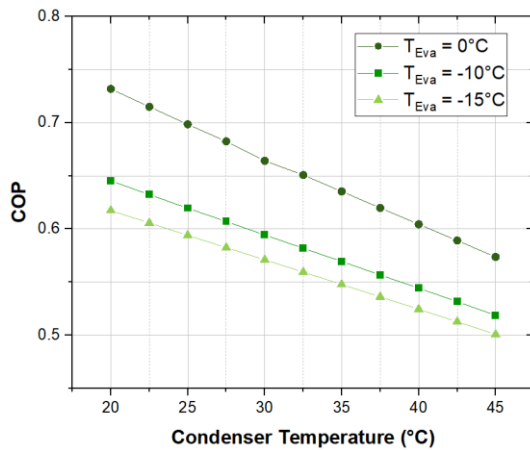


Fig. 6 COP vs Condenser Temperature.

refrigerant mass flow rate throughout the cycle. As a result, a greater amount of refrigerant is evaporated in the evaporator, producing a higher cooling effect and ultimately improving the overall efficiency of the system. The system exhibits a higher COP when the evaporator operates at 0°C. However, if the evaporator must operate at significantly lower temperatures (e.g., -10°C), the generator temperature must be further increased to offset the resulting decline in COP. This is because lower evaporator temperatures reduce the refrigerant's evaporation pressure, which diminishes the cooling capacity for a given mass flow rate. To maintain acceptable system performance under these conditions, additional thermal energy input at the generator is required to sustain the driving potential of the cycle. Similar behaviors have been reported by other authors, including Rabiei *et al.*, (2024), Zhu & Gu (2010) and Pandya *et al.* (2019).

Figure 6 illustrates the influence of condenser temperature on the coefficient of performance (COP) of the absorption refrigeration system for three different evaporator temperature settings (0°C, -10°C, and -15°C). As observed, the COP decreases with increasing condenser temperature and decreasing evaporator temperature. This behavior is consistent with findings reported in previous studies (Zhu & Gu, 2010), (Rabiei *et al.*, 2024), (Pandya *et al.*, 2019). The decline in COP with rising condenser temperature is attributed to the reduced effectiveness of heat rejection in the condenser, which increases the thermal load on the system and diminishes the thermodynamic driving force. Simultaneously, lower evaporator temperatures reduce the evaporation pressure of the refrigerant (NH<sub>3</sub>), thereby lowering the cooling capacity for a given mass

flow rate. Consequently, both effects combine to reduce system efficiency. These results underscore the importance of carefully balancing condenser and evaporator temperatures to sustain acceptable system performance under varying thermal conditions.

The effect of absorber temperature on the coefficient of performance (COP) for different evaporator temperature conditions is shown in Figure 7. In all cases, COP decreases progressively as the absorber temperature increases, reflecting the adverse impact of reduced absorption capacity and increased solution circulation ratio. At  $T_{eva} = 0\text{ C}$ , COP declines from approximately 0.75 at 20 °C to about 0.62 at 44 °C. A similar trend is observed for  $T_{eva} = -5\text{ C}$  and  $T_{eva} = -10\text{ C}$ , with overall lower COP values across the operating range.

This behavior can be attributed to the thermodynamic limitations associated with higher absorber temperatures. As the absorber temperature rises, the solubility of the refrigerant (NH<sub>3</sub>) in the working solution (NaSCN) decreases, reducing the effectiveness of the absorption process. Consequently, the weak solution exiting the absorber has a lower refrigerant content, diminishing the mass flow rate of refrigerant throughout the cycle and ultimately leading to a decline in cooling capacity and overall COP.

As observed in the Figure 8, the relationship between evaporator temperature and the coefficient of performance (COP) is directly proportional. An increase in evaporator temperature leads to higher COP values across all evaluated conditions. This behavior is explained by the reduction in the temperature gradient between the evaporator and the condenser, which decreases the system's thermal load and improves its efficiency. Conversely, at very low evaporator temperatures, the system requires more energy to extract heat, thereby reducing the COP. According to previous reports, an NH<sub>3</sub>-NaSCN chiller cannot operate when the evaporating temperature falls below -10 °C due to the risk of crystallization (Wu *et al.*, 2013). Therefore, in this study, the lower operating temperature was limited to -8 °C (Modi, Pandya, Kumar, *et al.*, 2020), (Cai *et al.*, 2016).

The influence of condenser and absorber temperatures on the COP is also significant. When both components operate at lower temperatures (e.g., 25 °C), the system achieves its highest COP throughout the entire range of evaporator temperatures analyzed. In contrast, when the condenser and absorber operate at elevated temperatures (e.g., 35 °C), the COP declines markedly indicating that the system cannot operate efficiently under such thermal conditions. This reduction in performance is primarily attributed to the increased thermal load on the condenser, which hampers heat rejection, and the diminished

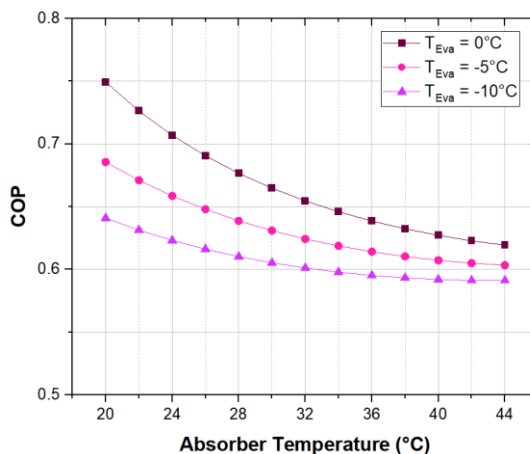


Fig. 7 COP vs Absorber Temperature.

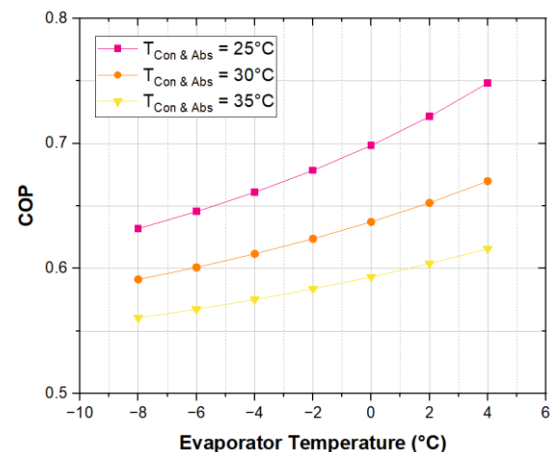


Fig. 8 COP vs Evaporator Temperature.

solubility of ammonia in the absorbent at higher absorber temperatures. These effects reduce the concentration gradient between the strong and weak solutions, limiting the refrigerant circulation rate and decreasing the cooling capacity of the system

4.2. Exergy analysis

Exergetic efficiency trends as a function of generator and evaporator temperatures are presented in Figure 9, with the black axis pair (bottom x-axis and left y-axis) representing  $\eta$  as a function of generator temperature for fixed evaporator and condenser/absorber conditions, and the red axis pair (top x-axis and right y-axis) showing  $\eta$  as a function of evaporator temperature for fixed generator and condenser/absorber conditions. For fixed condenser, absorber, and evaporator temperatures, the exergetic efficiency exhibits a non-monotonic trend with increasing generator temperature: it initially decreases up to approximately 120 °C and subsequently increases at higher values. This behavior results from the competing effects of generator temperature on the absorption cycle. In the lower to mid-range, a rise in generator temperature increases the solution circulation ratio and intensifies heat and mass transfer in the generator and absorber, which also enhances internal irreversibilities, thereby reducing efficiency. However, beyond 120 °C, the higher driving temperature significantly improves the desorption process and reduces the solution concentration difference between stages, leading to better exergy utilization and a recovery in efficiency.

Regarding the red curves (top x-axis and right y-axis in Figure 9), which represent the variation of exergetic efficiency with evaporator temperature under fixed generator, condenser, and absorber conditions, a consistent decreasing trend is observed as the evaporator temperature increases. This behavior can be attributed to two thermodynamic mechanisms. First, raising the evaporator temperature reduces the temperature lift between the evaporator and the absorber/condenser, thereby decreasing the cooling effect relative to the thermal energy supplied to the generator. Second, at elevated evaporator temperatures, the absorption process becomes less effective, requiring higher solution circulation rates to sustain the cycle. This increase in circulation exacerbates internal irreversibilities associated with heat and mass transfer, ultimately lowering the system’s overall exergetic efficiency.

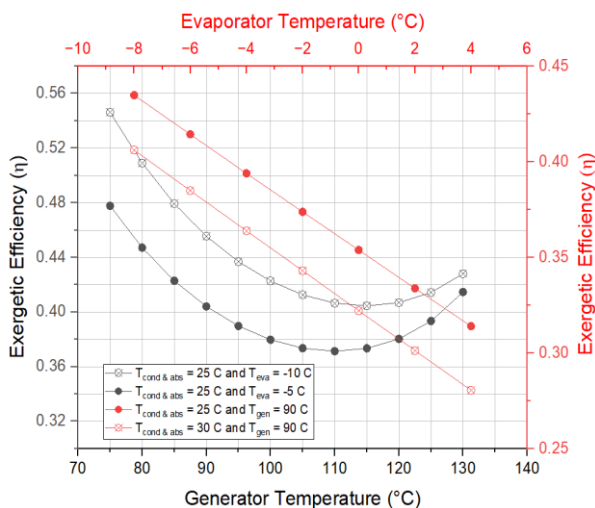


Fig. 9 Exergetic efficiency of the system ( $\eta$ ).

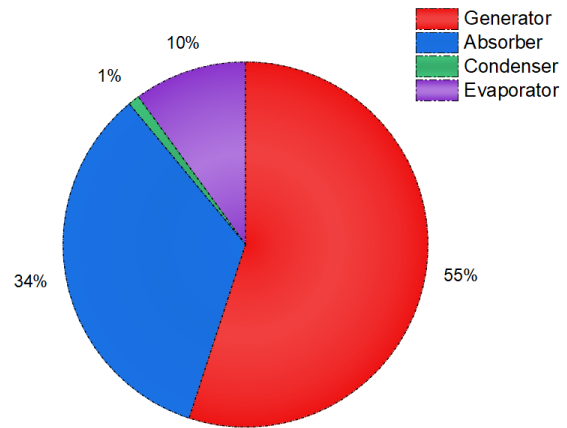


Fig. 10 Exergy destruction by component.

Figure 10 shows the distribution of exergy destruction by component, evaluated under the initial operating conditions. The components are ranked in descending order of exergy destruction as follows: generator, absorber, evaporator, and condenser. The generator (55%) and absorber (34%) account for the largest shares of exergy destruction. This predominance is attributed to the complex heat- and mass-transfer interactions occurring within these components. In the generator, the simultaneous processes of ammonia desorption, solution heating, and fluid mixing take place under significant temperature and concentration gradients, leading to pronounced irreversibilities. Similarly, in the absorber, the exothermic absorption of ammonia into the solution involves substantial heat rejection and mixing under non-equilibrium conditions, which further contributes to exergy losses. This distribution is consistent with findings reported in the literature, where the generator and absorber are consistently identified as the primary sources of irreversibility in absorption refrigeration cycles (Yang *et al.*, 2021).

4.3. Solar-assisted system analysis

A subsystem consisting of solar collectors and a water storage tank, which transfers heat from the collectors to the generator, was coupled to the initial system. This configuration was evaluated considering the average hourly solar irradiation for five cities in the Caribbean region of Colombia (Fig 11).

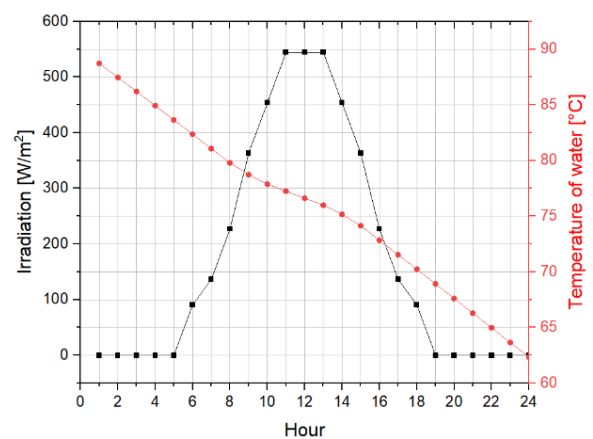


Fig. 11 Evolution of water temperature with average hourly irradiation.

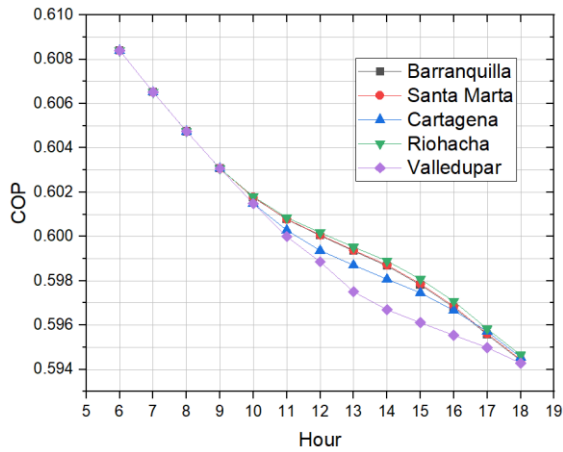


Fig. 12 Evolution of COP with average hourly irradiation.

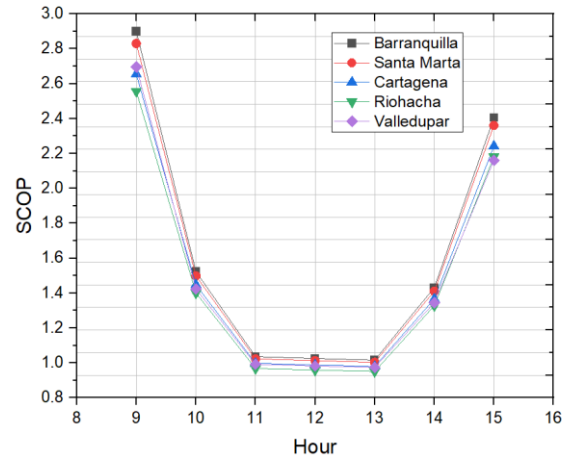


Fig. 14 Evolution of SCOP with average hourly irradiation.

The behavior of the water temperature in relation to the average daily solar irradiation is shown in Figure 11. The temperature in the 5 m<sup>3</sup> storage tank, which determines the thermal energy supplied to the generator, decreases over time as a result of three combined factors: the continuous heat demand of the generator, thermal losses from the tank to the environment, and the insufficient heat production from the solar collectors for the installed collector area. Figure 11 presents the average values for the analyzed cities in the Colombian Caribbean region, as their individual profiles exhibited similar trends; however, a subsequent analysis will address the individual behavior of COP, SCOP, and exergetic efficiency for each city. The overall variation in these indicators remains relatively limited, as the most significant changes in COP, SCOP, and exergy efficiency typically occur within the optimal generator temperature range of 90–110 °C. This range could not be reached in this study due to the use of water as the working fluid in the storage tank and collector model, which constrains operation below this temperature threshold. Nevertheless, these findings provide valuable insights for guiding future dynamic analyses of system performance under variable temperature conditions.

The decrease in the temperature supplying the generator leads to a gradual reduction in COP, as shown in Figure 12. This reduction is mainly due to the lower thermal driving potential for the desorption process, which decreases the amount of refrigerant effectively separated and increases the solution circulation ratio, ultimately lowering the cycle’s performance. Valledupar shows the largest COP drop because it has the lowest average hourly solar irradiation, which causes a sharper

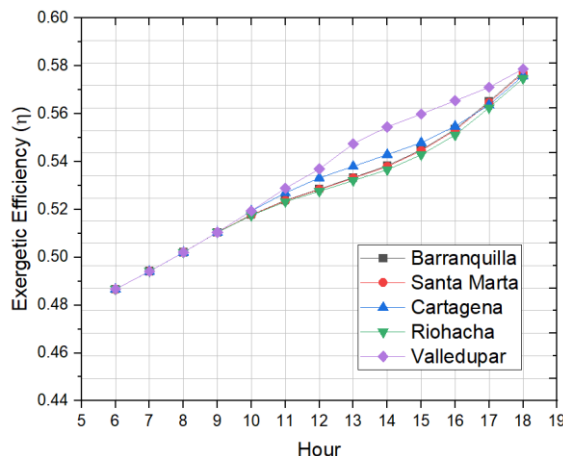


Fig. 13 Evolution of η with average hourly irradiation.

decrease in the storage tank temperature. In contrast, Riohacha, Santa Marta, and Barranquilla, which have similar and higher irradiation levels, present a more moderate COP decrease, indicating better resistance to performance losses.

On the other hand, Figure 13 shows how the exergetic efficiency increases as the operating temperature difference between the generator and the evaporator decreases (with the evaporator operating at a fixed temperature in the simulation). This behavior can be explained by the reduction in irreversibilities within the cycle, as a smaller temperature difference lowers the entropy generation associated with heat transfer processes, particularly in the generator and absorber. Consequently, the system converts a greater proportion of the supplied thermal energy into useful cooling, leading to an overall improvement in exergetic efficiency. Cities with lower average irradiation, which exhibit a faster decrease in generator temperature and a steeper decline in COP, show the greatest increase in exergetic efficiency due to the reduction of irreversibilities.

The solar COP (SCOP) was calculated for the period between 09:00 and 15:00, coinciding with the hours of highest solar irradiation. It is observed in Figure 14 that SCOP decreases toward midday as a result of the increased heat gain from the collectors, which reduces the ratio of useful cooling to thermal input when solar irradiation reaches its peak, and subsequently increases again as solar radiation declines in the afternoon. Riohacha exhibits the lowest SCOP, which is attributed to its higher solar gain compared to the other five cities, followed by Valledupar and Cartagena.

#### 4.4. Optimization and Surface Response Method

A factorial experimental design was developed, and the response surface methodology was applied through second-order polynomial regression, resulting in the analysis of variance presented in Table 4. Given the orthogonality of the experimental design, the sequential and adjusted sums of squares yielded identical numerical values. Therefore, for the sake of clarity, only the adjusted sums of squares (Adj SS) are reported in this study, as they provide the most relevant information for interpreting the model.

The analysis of variance (ANOVA) revealed that the fitted model was highly significant ( $F = 766.31; p < 0.0001$ ), explaining 98.36% of the total variability in the coefficient of performance (COP). The linear effects accounted for the largest proportion of the variation (85.77%), with the generator temperature contributing the most (39.37%), followed by the condenser temperature (31.22%) and, to a lesser extent, the evaporator

**Table 4**  
Analysis of variance for the cop regression model

Source	DF	Contribution	Adj SS	Adj MS	F-Value
<b>Model</b>	<b>9</b>	<b>98.36%</b>	<b>1.29689</b>	<b>0.144099</b>	<b>766.31</b>
<b>Linear</b>	<b>3</b>	<b>85.77%</b>	<b>1.1309</b>	<b>0.376967</b>	<b>2004.68</b>
Tgen	1	39.37%	0.51916	0.51916	2760.86
Tcond	1	31.22%	0.41162	0.411618	2188.96
Teva	1	15.18%	0.20012	0.200122	1064.24
<b>Quadratic</b>	<b>3</b>	<b>3.07%</b>	<b>0.04049</b>	<b>0.013496</b>	<b>71.77</b>
Tgen*Tgen	1	2.37%	0.03119	0.031187	165.85
Tcon*Tcon	1	0.53%	0.007	0.006996	37.2
Teva Teva	1	0.17%	0.0023	0.002304	12.25
<b>Two-way interaction</b>	<b>3</b>	<b>9.52%</b>	<b>0.1255</b>	<b>0.041835</b>	<b>222.48</b>
Tgen*Tcon	1	5.44%	0.07167	0.071671	381.14
Tgen*Teva	1	2.52%	0.03318	0.03318	176.45
Tcon*Teva	1	1.57%	0.02065	0.020654	109.84
<b>Error</b>	<b>115</b>	<b>1.64%</b>	<b>0.02162</b>	<b>0.000188</b>	
<b>Total</b>	<b>124</b>	<b>100.00%</b>			

temperature (15.18%). Additionally, the quadratic terms (3.07%) and the two-way interaction effects (9.52%) were statistically significant ( $p < 0.05$ ), indicating the presence of curvature in the response surface and combined effects among the evaluated factors.

These findings confirm that the generator temperature is the dominant factor influencing the linear behavior of the COP, followed by the condenser and evaporator temperatures. Moreover, the response variable (COP) is also affected by nonlinear and interaction effects among the operating variables, which supports the use of a second-order polynomial model to accurately describe the system. The resulting predictive equation is presented below, achieving a coefficient of determination ( $R^2$ ) of 97.80%

$$COP = 0.846 + 0.00005 \cdot T_{gen} - 0.01126 \cdot T_{con} + 0.00958 \cdot T_{eva} + 0.000094 \cdot T_{gen}^2 + 0.000715 \cdot T_{con}^2 + 0.000411 \cdot T_{eva}^2 - 0.000479 \cdot T_{gen} \cdot T_{con} + 0.000326 \cdot T_{gen} \cdot T_{eva} - 0.001028 \cdot T_{con} \cdot T_{eva} \quad (31)$$

In order to assess the interaction between the two temperatures with the greatest influence on COP, a response surface was generated at an intermediate evaporator temperature of  $T_{eva} = 0$ . The results observed in Figure 15 show that COP increases consistently with higher generator temperatures, highlighting the positive effect of a stronger

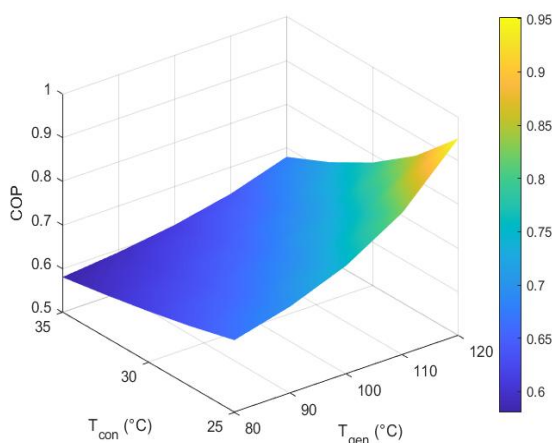


**Fig. 15** Effect of Generator and Condenser Temperatures on COP at  $T_{eva} = 0$  C.

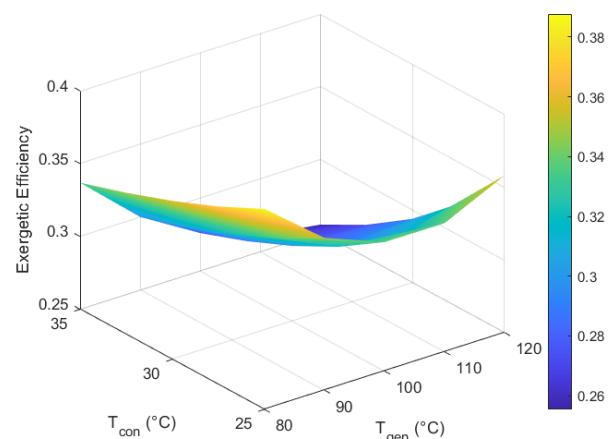


**Fig. 16** Effect of Generator and Condenser Temperatures on  $\eta$  at  $T_{eva} = 0$  C.

thermal driving potential on the desorption process. Conversely, an increase in condenser temperature reduces COP, as it raises the thermal load associated with heat rejection. The combined effect of these parameters delineates a performance gradient, with the highest COP values occurring at high generator and low condenser temperatures.

To analyze the behavior of exergetic efficiency, a response surface was generated at an intermediate evaporator temperature of  $T_{eva} = 0$  considering the combined influence of generator and condenser temperatures. The results shown in Figure 16 reveal a non-monotonic dependence on generator temperature: at lower generator temperatures values,  $\eta$  decreases slightly as generator temperature increases. This initial decline is explained by the rise in solution circulation ratio and intensification of heat transfer irreversibilities within the generator and absorber, which outweigh the thermodynamic gains from higher desorption rates. However, at higher generator temperatures values, exergetic efficiency recovers, as the improved thermal driving potential enhances refrigerant desorption and reduces the concentration difference between the strong and weak solution streams, improving exergy utilization. In contrast, increasing condenser temperature consistently lowers  $\eta$ , since rejecting heat at a higher sink temperature raises irreversibilities associated with the condensation process. To determine the optimal operating point considering the simultaneous maximization of COP and

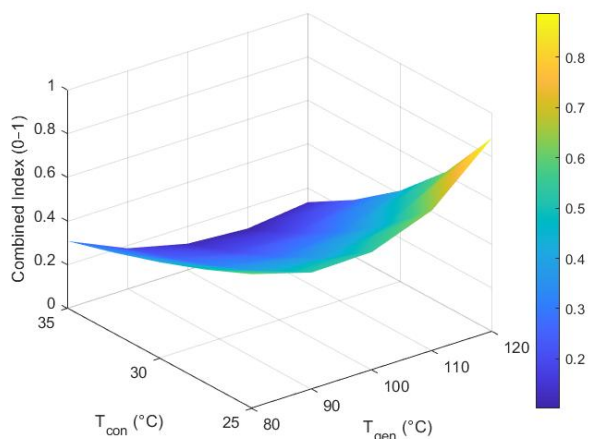


**Fig. 17** Effect of Generator and Condenser Temperatures on the Combined Index at  $T_{eva} = 0\text{ }^{\circ}\text{C}$

exergetic efficiency, a combined performance index was developed. This index was constructed by assigning equal weights (50 %) to the normalized COP and the normalized exergetic efficiency ( $\eta$ ), ensuring that both energy- and exergy-based performance perspectives were incorporated with equal importance. This approach helps identify operating conditions that balance the two key performance indicators, using a multi-criteria evaluation method that offers a clear and practical tool for decision-making. Using this index, a response surface was generated, which could be observed in Figure 17, to illustrate the combined effect of generator and condenser temperatures at an intermediate evaporator temperature  $T_{eva} = 0\text{ }^{\circ}\text{C}$ .

## 5. Conclusions

This study presented a thermodynamic and exergetic evaluation of a single-effect absorption refrigeration system using  $\text{NH}_3\text{-NaSCN}$  as the working pair, integrated with a solar collector under the specific climatic conditions of Barranquilla, Colombia. The validation process confirmed the accuracy of the thermodynamic model for the  $\text{NH}_3\text{-NaSCN}$  solution, while also highlighting the need to improve the correlations used for the properties of pure ammonia.

The analysis of the influence of operating temperatures from Figure 5 to Figure 8 showed that increasing the generator temperature from  $75\text{ }^{\circ}\text{C}$  to  $120\text{ }^{\circ}\text{C}$  enhanced the coefficient of performance (COP) by up to 46.15% for an evaporator temperature of  $0\text{ }^{\circ}\text{C}$ , as a result of the greater refrigerant desorption capacity and the increased concentration gradient between the strong and weak solutions. Beyond this range, further increases in generator temperature had a negligible effect on COP. In contrast, raising the condenser temperature from  $20\text{ }^{\circ}\text{C}$  to  $45\text{ }^{\circ}\text{C}$  reduced the COP by approximately 20.54%, while increasing the absorber temperature from  $20\text{ }^{\circ}\text{C}$  to  $44\text{ }^{\circ}\text{C}$  caused a decrease of about 16 % under the same evaporator conditions, primarily due to the reduced solubility of ammonia in the absorbent solution. Furthermore, increasing the evaporator temperature from  $-8\text{ }^{\circ}\text{C}$  to  $4\text{ }^{\circ}\text{C}$  improved the COP by up to 14.6%, owing to the reduced temperature lift between the evaporator and condenser, which in turn lowered the thermal load and improved the overall thermodynamic performance of the cycle.

The exergy destruction distribution indicates that the generator accounts for 55 % of the total losses, followed by the

absorber with 34 %, while the evaporator and condenser exhibit significantly lower values. This suggests that optimization strategies should primarily focus on reducing irreversibilities in these two components to achieve substantial improvements in overall system efficiency. With respect to generator temperature, the exergetic efficiency exhibits a non-monotonic trend: under fixed sink conditions, it decreases slightly up to approximately  $120\text{ }^{\circ}\text{C}$  and subsequently recovers at higher temperatures, reflecting the trade-off between the increase in irreversibilities due to higher solution circulation rates and the enhancement of refrigerant desorption under larger thermal gradients. In contrast, the evaporator temperature shows a monotonic decrease in exergetic efficiency, from approximately 0.50 to 0.31 at  $T_{gen} = 90\text{ }^{\circ}\text{C}$  and  $T_{cond} = T_{abs} = 25\text{ }^{\circ}\text{C}$ , corresponding to a 38 % reduction. This decline is attributed to the reduced fraction of useful exergy as the effective temperature lift of the cycle decreases and the irreversibilities associated with heat and mass transfer processes increase, highlighting the importance of maintaining the evaporator within lower temperature ranges when aiming to maximize exergetic efficiency.

The integration of the solar subsystem enabled the system to operate within a stable range throughout the day; however, variations in solar irradiance induced fluctuations in both COP and SCOP. The average COP decline across all cities was approximately 3 % over the course of the day. However, in high-irradiance locations such as Riohacha, Santa Marta, and Barranquilla, the reduction was less pronounced, whereas in Valledupar the COP decreased more sharply, converging toward a similar final value despite starting from a higher initial level of performance loss. Nevertheless, the use of water as the working fluid in the solar collectors imposes a limitation on achieving the generator temperature range generally associated with maximum system efficiency, typically between  $95\text{ }^{\circ}\text{C}$  and  $120\text{ }^{\circ}\text{C}$ . Under the current configuration, the generator temperature remained below  $90\text{ }^{\circ}\text{C}$  for most of the operational period, thereby preventing the system from fully exploiting the optimal thermodynamic potential of the  $\text{NH}_3\text{-NaSCN}$  cycle. A promising improvement strategy would involve employing an alternative heat transfer fluid with a higher boiling point, such as thermal oils, pressurized water, or molten salts, which could increase the generator inlet temperature by up to 20–25 %, extend the operational range of the collectors, reduce thermal losses, and allow the generator to consistently operate within its optimum efficiency range.

The analysis of variance demonstrated that generator temperature was the dominant factor influencing the COP, contributing 39.37 % of the total variation, followed by condenser temperature (31.22 %) and evaporator temperature (15.18 %). Together, these linear effects accounted for 85.77 % of the total variability, indicating that the system's energy performance is highly sensitive to individual component temperature levels. Quadratic effects (3.07 %) and two-way interaction effects (9.52 %) collectively explained 12.59 % of the variation, confirming the relevance of nonlinearities and coupled parameter influences in accurately predicting system behavior. The regression model achieved a coefficient of determination of  $R^2 = 98.36\%$ , indicating that it explains nearly all of the observed variability in COP. This high explanatory power confirms that the model effectively captures the relationship between the operating temperatures and system performance, making it a solid tool for guiding operational adjustments and design improvements.

The surface responses exposed in Figures 15, 16 and 17 show that COP increases with higher generator and lower condenser temperatures, while exergetic efficiency exhibits a non-monotonic dependence on generator temperature and

decreases with increasing condenser temperature. The combined performance index highlights that the high  $T_{gen}$  and low  $T_{cond}$  region offers the optimal balance between energy and exergy performance, serving as a practical guide for selecting operating conditions.

The results provide a valuable basis for future improvements in the design of solar-assisted absorption systems and support the adoption of  $\text{NH}_3\text{-NaSCN}$  as an efficient and cost-effective solution for renewable refrigeration, particularly in regions with high solar energy availability. Future research could focus on optimizing the components with the highest exergy destruction and incorporating economic indicators to extend this analysis toward an exergoeconomic approach.

## Acknowledgments

The authors gratefully acknowledge the support provided by Universidad de la Costa (CUC) for its contribution to the development of this research.

**Author Contributions:** J.C.C.O.: Conceptualization, methodology, formal analysis, writing—original draft preparation. N.D.C.: Supervision, resources, investigation, project administration. V.C.C.: Writing—review and editing, project administration, validation. D.S.P.: Writing—review and editing, project administration, validation. H.A.G.: Data curation, visualization. A.R.T.: Validation, administrative support, review of final manuscript. All authors have read and agreed to the published version of the manuscript.

**Funding:** The authors received no financial support for the research, authorship, and/or publication of this article.

**Conflicts of Interest:** The authors declare no conflicts of interest.

## References

- Ali, M., & Evans, S. (2025). The impact of best practice on energy efficiency in industrial decarbonization policy. *Energy Policy*, 204, 114632. <https://doi.org/10.1016/j.enpol.2025.114632>
- Alshammari, N. K. (2025). An examination of the exergy and energy of a solar powered absorption cooling systems in the Riyadh climate. *Journal of Engineering Research*. <https://doi.org/10.1016/j.jer.2025.03.006>
- Bastos, L. K., & Almeida, A. G. S. (2024). Simulation of a solar absorption air conditioning system for a tropical wet region in Brazil. *World Review of Science, Technology and Sustainable Development*, 20(1), 35–46. <https://doi.org/10.1504/WRSTSD.2024.136009>
- Bell, I. H., Wronski, J., Quoilin, S., & Lemort, V. (2014). Pure and Pseudo-pure Fluid Thermophysical Property Evaluation and the Open-Source Thermophysical Property Library CoolProp. *Industrial & Engineering Chemistry Research*, 53(6), 2498–2508. <https://doi.org/10.1021/ie4033999>
- Bouzyan, L., Toub Blanc, C., & Ousegui, A. (2023). Modeling of a LiBr- $\text{H}_2\text{O}$  absorption air conditioner system driven by a solar flat plate collector. *E3S Web of Conferences*, 469, 00049. <https://doi.org/10.1051/e3sconf/202346900049>
- Cabrera César, J., Caratt Ortiz, J., Ochoa, G. V., Restrepo, R. R., & Alvarez, J. R. N. (2021). A New Computational Tool for the Development of Advanced Exergy Analysis and LCA on Single Effect LiBr- $\text{H}_2\text{O}$  Solar Absorption Refrigeration System. *Lubricants*, 9(8), 76. <https://doi.org/10.3390/lubricants9080076>
- Cai, D., He, G., Tian, Q., & Tang, W. (2014). Exergy analysis of a novel air-cooled non-adiabatic absorption refrigeration cycle with  $\text{NH}_3\text{-NaSCN}$  and  $\text{NH}_3\text{-LiNO}_3$  refrigerant solutions. *Energy Conversion and Management*, 88, 66–78. <https://doi.org/10.1016/j.enconman.2014.08.025>
- Cai, D., Jiang, J., He, G., Li, K., Niu, L., & Xiao, R. (2016). Experimental evaluation on thermal performance of an air-cooled absorption refrigeration cycle with  $\text{NH}_3\text{-LiNO}_3$  and  $\text{NH}_3\text{-NaSCN}$  refrigerant solutions. *Energy Conversion and Management*, 120, 32–43. <https://doi.org/10.1016/j.enconman.2016.04.089>
- Camara, S., & Sulin, A. B. (2024). Reducing cooling water consumption in a solar absorption chiller for Mali climates. *Energy Efficiency*, 17(6), 57. <https://doi.org/10.1007/s12053-024-10240-x>
- Duffie, J. A., & Beckman, W. A. (2013). *Solar Engineering of Thermal Processes*. Wiley. <https://doi.org/10.1002/9781118671603>
- Farshi, L. G., Infante Ferreira, C. A., Mahmoudi, S. M. S., & Rosen, M. A. (2014). First and second law analysis of ammonia/salt absorption refrigeration systems. *International Journal of Refrigeration*, 40, 111–121. <https://doi.org/10.1016/j.ijrefrig.2013.11.006>
- Gao, K., Wu, J., Bell, I. H., Harvey, A. H., & Lemmon, E. W. (2023). A Reference Equation of State with an Associating Term for the Thermodynamic Properties of Ammonia. *Journal of Physical and Chemical Reference Data*, 52(1). <https://doi.org/10.1063/5.0128269>
- Infante Ferreira, C. A. (1984). Thermodynamic and physical property data equations for ammonia-lithium nitrate and ammonia-sodium thiocyanate solutions. *Solar Energy*, 32(2), 231–236. [https://doi.org/10.1016/S0038-092X\(84\)80040-7](https://doi.org/10.1016/S0038-092X(84)80040-7)
- Isaza-Roldan, C. A., & Cardona-Gil, J. A. (2014). *Sistema de control de aire acondicionado con energía solar y ciclo de refrigeración por absorción*. <https://www.researchgate.net/publication/327187099>
- Kabir, E., Kumar, P., Kumar, S., Adelodun, A. A., & Kim, K.-H. (2018). Solar energy: Potential and future prospects. *Renewable and Sustainable Energy Reviews*, 82, 894–900. <https://doi.org/10.1016/j.rser.2017.09.094>
- Kerme, E. D., Chafidz, A., Agboola, O. P., Orfi, J., Fakeeha, A. H., & Al-Fatesh, A. S. (2017). Energetic and exergetic analysis of solar-powered lithium bromide-water absorption cooling system. *Journal of Cleaner Production*, 151, 60–73. <https://doi.org/10.1016/j.jclepro.2017.03.060>
- Lemmon, E. W., McLinden, M. O., & Wagner, W. (2009). Thermodynamic Properties of Propane. III. A Reference Equation of State for Temperatures from the Melting Line to 650 K and Pressures up to 1000 MPa. *Journal of Chemical & Engineering Data*, 54(12), 3141–3180. <https://doi.org/10.1021/je900217v>
- Mardones Barrientos, C. (2016). *Comparación entre los ciclos de refrigeración por compresión de vapor y absorción mediante la primera y segunda ley de la termodinámica en aplicaciones de climatización y refrigeración* [Universidad de Chile]. <https://repositorio.uchile.cl/handle/2250/142073>
- Modi, N., Pandya, B., Kumar, V., & Patel, J. (2020). Dynamic Performance Investigation of Single-Effect  $\text{NH}_3 + \text{LiNO}_3$  and  $\text{NH}_3 + \text{NaSCN}$  Solar Cooling Cycles: A Case Study for Western Indian Climate. *Journal of Solar Energy Engineering*, 142(5). <https://doi.org/10.1115/1.4046604>
- Modi, N., Pandya, B., & Patel, J. (2020). Investigation of an Energy Source Temperature for  $\text{NH}_3 + \text{NaSCN}$  and  $\text{NH}_3 + \text{LiNO}_3$  Absorption Refrigeration Systems. *Journal of Energy Resources Technology*, 142(10). <https://doi.org/10.1115/1.4047017>
- Ngock, G. R. H., Tamba, J. G., Djanna, F., & Ndjakomo, S. E. (2022). Analysis and improvement of the efficiency of  $\text{NH}_3\text{-NaSCN}$  single effect absorption cooling system. *Heliyon*, 8(11), e11635. <https://doi.org/10.1016/j.heliyon.2022.e11635>
- Ngock, R. G., Tamba, J. G., Ndjakomo, S., Djanna, F., & Ndame, M. (2020). Thermodynamic Analysis of the Performance of a Single-Effect Absorption Refrigeration System Using the Ammonia/Sodium Thiocyanate Couple. *Open Journal of Energy Efficiency*, 09(01), 53–63. <https://doi.org/10.4236/ojee.2020.91004>
- Niño Villamizar, Y. A., Nieves Plata, M. E., & Cortés Jiménez, C. A. (2023). Desafíos de la transición energética sostenible. *Revista Facultad de Ciencias Económicas*, 31(2), 137–158. <https://doi.org/10.18359/rfce.6423>
- Pandya, B., Modi, N., Kumar, V., Upadhyai, R., & Patel, J. (2019). Performance comparison and optimal parameters evaluation of solar-assisted  $\text{NH}_3\text{-NaSCN}$  and  $\text{NH}_3\text{-LiNO}_3$  type absorption cooling system. *Journal of Thermal Analysis and Calorimetry*, 135(6), 3437–3452. <https://doi.org/10.1007/s10973-018-7561-8>
- Rabiei, R., Bodaghi, M. B., & Kazemi, A. (2024). Exergy and exergoeconomic comparative analysis of three  $\text{NH}_3\text{-NaSCN}$

- absorption refrigeration cycles driven by solar collector. *Journal of the Brazilian Society of Mechanical Sciences and Engineering*, 46(6). <https://doi.org/10.1007/s40430-024-04870-6>
- Ramírez Álvarez, D. J., Tapia Vertel, A. F., Lancheros Suárez, V. J., Espitia Sanjuán, L. A., & González Dória, Y. E. (2015). Simulación y análisis de un sistema de refrigeración por absorción solar intermitente. *Revista de Ingeniería*, (43), 32–39. <https://doi.org/10.16924/riua.v0i43.872>
- Raugei, M., & Frankl, P. (2009). Life cycle impacts and costs of photovoltaic systems: Current state of the art and future outlooks. *Energy*, 34(3), 392–399. <https://doi.org/10.1016/j.energy.2009.01.001>
- Shankar, R., Srinivas, T., & Reddy, B. V. (2017). Thermodynamic evaluations of solar cooling cogeneration cycle using NaSCN–NH<sub>3</sub> mixture. *Applied Solar Energy*, 53(3), 267–275. <https://doi.org/10.3103/S0003701X17030100>
- Sharma, S., & Maithani, R. (2026). Multi-objective optimization of solar air heater having centerline perforated sine wave baffles using experimental and machine learning based approaches. *Experimental Heat Transfer*, 39(1), 1–23. <https://doi.org/10.1080/08916152.2024.2430592>
- Siddiqui, M. A. (1993). Optimum generator temperatures in four absorption cycles using different sources of energy. *Energy Conversion and Management*, 34(4), 251–266. [https://doi.org/10.1016/0196-8904\(93\)90109-N](https://doi.org/10.1016/0196-8904(93)90109-N)
- Soto Robles, A. (2018). *Evaluación y optimización energética y exergética de sistemas de refrigeración por absorción*. <https://oa.upm.es/50040/>
- Sun, D.-W. (1998). Comparison of the performances of NH<sub>3</sub>-H<sub>2</sub>O, NH<sub>3</sub>-LiNO<sub>3</sub> and NH<sub>3</sub>-NaSCN absorption refrigeration systems. *Energy Conversion and Management*, 39(5–6), 357–368. [https://doi.org/10.1016/S0196-8904\(97\)00027-7](https://doi.org/10.1016/S0196-8904(97)00027-7)
- Takalkar, G., & Sleiti, A. K. (2022). Comprehensive performance analysis and optimization of 1,3-dimethylimidazolium dimethylphosphate-water binary mixture for a single effect absorption refrigeration system. *Frontiers in Energy*, 16(3), 521–535. <https://doi.org/10.1007/s11708-021-0720-9>
- Toscano, A. R., Ortiz, J. C., Armas Calderón, N. De, & Alarcón, M. G. (2024). Technical evaluation of solar-activated absorption refrigeration systems and operating conditions: a case study in Culiacán-Mexico. *Procedia Computer Science*, 238, 1015–1022. <https://doi.org/10.1016/j.procs.2024.06.128>
- Toscano, A. R., Ortiz, J. C., & Calderón, N. D. A. (2024). Technical analysis and evaluation of the energy performance of solar-activated absorption refrigeration systems: Case of the Caribbean Coast of Colombia. *Procedia Computer Science*, 231, 471–477. <https://doi.org/10.1016/j.procs.2023.12.236>
- Velázquez Martí, B. (2017). *Sistemas de refrigeración por absorción* [Departamento de Ingeniería Rural y Agroalimentaria Universitat Politècnica de València]. <https://riunet.upv.es/bitstream/handle/10251/193307/Velazquez%20-%20Sistemas%20de%20refrigeracion%20por%20absorcion%20SRA.pdf?sequence=1>
- Venegas, M., García-Hernando, N., Zacarias, A., & de Vega, M. (2020). Performance of a Solar Absorption Cooling System Using Nanofluids and a Membrane-Based Microchannel Desorber. *Applied Sciences*, 10(8), 2761. <https://doi.org/10.3390/app10082761>
- Waghare, P., & Sathyabhama, A. (2022). Performance analysis of ammonia-based vapour absorption refrigeration system. *Materials Today: Proceedings*, 51, 1503–1509. <https://doi.org/10.1016/j.matpr.2021.10.279>
- Wu, W., Wang, B., Shi, W., & Li, X. (2013). Crystallization Analysis and Control of Ammonia-Based Air Source Absorption Heat Pump in Cold Regions. *Advances in Mechanical Engineering*, 5. <https://doi.org/10.1155/2013/140341>
- Yang, L., Huang, S., Lu, Z., Gong, Y., & Li, H. (2021). Application and discussion on entransy analysis of ammonia/salt absorption heat pump systems. *International Journal of Low-Carbon Technologies*, 16(3), 977–986. <https://doi.org/10.1093/ijlct/ctab027>
- Zhu, L., & Gu, J. (2010). Second law-based thermodynamic analysis of ammonia/sodium thiocyanate absorption system. *Renewable Energy*, 35(9), 1940–1946. <https://doi.org/10.1016/j.renene.2010.01.022>

